Desalination and Water Treatment
www.deswater.com

doi: 10.5004/dwt.2020.26271

206 (2020) 416–428
December

PSO-based integration navigation and LiDAR-based remote sensing algorithms for 3D agriculture digital modeling with light multi-rotor UAV

Guangqi Wang[a,†], Yu Han[b,c,†], Jian Chen[a,*], Hao Meng[a], Shubo Wang[a], Zichao Zhang[a]

[a]*College of Engineering, China Agricultural University, Beijing 100083, China, email: jchen@cau.edu.cn (J. Chen)*
[b]*College of Water Resources & Civil Engineering, China Agricultural University, Beijing 100083, China, email: yhan@cau.edu.cn (Y. Han)*
[c]*State Key Laboratory of Information Engineering in Surveying, Mapping and Remote Sensing, Wuhan University, Wuhan 430079, China*

Received 27 July 2019; Accepted 15 January 2020

ABSTRACT

Traditional remote sensing methods have short revisiting cycles and poor timeliness, it is difficult to apply in agriculture because of its high cost. In order to solve the above problems and meet the requirements of digital agricultural development. This paper focuses on the optimization of integrated navigation algorithms and the establishment of a three-dimensional digital model of a ground specific target for multi-rotor unmanned aerial vehicle remote sensing at low altitude. Firstly, aiming at the poor positioning accuracy of the traditional small airborne integrated navigation systems, a linear decreasing particle swarm optimization (PSO) algorithm is used to set the optimal noise covariance matrix Q and R. The global optimization characteristics of PSO algorithm is used to optimize Q and R jointly. Secondly, a set of filtering and interpolation algorithms for processing point cloud data of airborne LiDAR remote sensing systems are integrated. The method of extracting irrigation canal characteristic lines is proposed; a new threshold selection method is used to improve the accuracy of irrigation canal characteristic line extraction. Finally, the experiment shows that the convergence curve of the iteration reaches the global optimum after 100 iterations, the integrated navigation algorithm optimized by linear decreasing PSO has a strong robust ability. The variance of longitude error and latitude error is 0.00076 and 0.00041. The three-dimensional digital model of wheat in two different periods, *Euonymus japonicus* and *Anemone* was established in MATLAB. The height error of the three-dimensional digital model of the above crops is 4.78%, 4.46%, 5.72%, and 7.31%. An irrigation canal was successfully extracted and its three-dimensional digital model was established. The errors of average depth and width between the three-dimensional model and the true value are 4.42% and 4.56%.

Keywords: LiDAR remote sensing; Multi-rotor unmanned aerial vehicle; Particle swarm optimization; Ecological irrigation canal; Ground crop; Point cloud data

1. Introduction

LiDAR is a promising active remote sensing technology that has been applied in many scientific fields to extract key parameters of biophysics [1–3]. As one of the most effective active remote sensing technologies, LiDAR has great advantages in obtaining the target physical parameters [4]. Airborne laser scanner (ALS) and terrestrial laser scanner are the two most common platforms of LiDAR [5]. The data obtained by LiDAR remote sensing can achieve better observation of individual plants, which is unmatched by the traditional two-dimensional data obtained by images [6–9]. LiDAR has been widely used in many fields. LiDAR can provide information about the horizontal and vertical structure of the forest and has been successfully used to estimate the height of the canopy [10–12]. There are also many research results for the establishment of laser radar three-dimensional digital model and target extraction. Alexander et al. [13] studied the effect of slope and canopy

* Corresponding author.

† These authors contributed equally to this work.

characteristics on treetop and tree height estimation of ALS data for complex terrain and complex canopy characteristics in forests. The same method using the digital surface model minus the digital terrain model to derive the canopy height model can be used as a reference for estimating the plant height on the canal slope. He et al. [14] used multiple 2D laser radars to establish a 3D environment, so calibrating the geometric transformation between multiple sensors and carrier frames is a research focus. This study proposes a method that can calibrate multiple 2D laser radars, a calibration algorithm based on multi-type geometric features is proposed, which is to extract features such as points, lines, surfaces and quadrics from the point cloud data of each LiDAR sensor to achieve matching of multiple radar data. The segmentation method of building top surface area growth of the building with the laser radar point cloud data is constructed. The segmentation of the top surface of the building can be accurately realized. Because the intensity information of point cloud has certain separability, the classification of ground materials can be realized [15]. Cao et al. [16] aimed to associate the active remote sensing with the passive remote sensing to retrieve the forest canopy cover using the linear spectrum decomposition model and geo-optical model, which makes forest canopy coverage easier to retrieve. Fayad et al. [17], Wang et al. [18], Xiang et al. [19], Paris and Bruzzone [20] studied the application of LiDAR remote sensing data in forest canopy detection and single-wood detection, including point cloud difference and filtering. However, current airborne and satellite LiDAR systems are unable to provide data on a regional and global scale. The unmanned aerial vehicle (UAV) is highly flexible and the UAV-equipped LiDAR remote sensing system can quickly and simultaneously collect data from the same area. The airborne LiDAR system consists of two parts: LiDAR and integrated navigation system. In order to improve the accuracy of remote sensing operations, the optimization of the algorithm can further improve the accuracy when the hardware cannot be improved. For the past several decades, there has been a great change in integrated navigation systems. In order to exploit the complementary characteristics of different sensors, different navigation sensors were combined [21,22]. However, the global position system/inertial navigation system (GPS/INS) integrated navigation system is still the most sophisticated navigation system, which has been widely used to provide the geographical position, velocity, and attitude of a vehicle. Traditional GPS/INS integrated systems can bridge the GPS gaps and the navigation capability is strongly dependent on the performances of standalone INS [23]. The GPS/INS integration system is designed by employing an adaptive filter that can estimate measurement noise variance using the residual of the measurement [24]. Ultra-tightly coupled method is the best but it is too complicated [25–27]. In Wang et al. [28], a combined navigation method for small agricultural drones is proposed. The feedback correction method is used in the paper. Finally, the experimental results show that the filtered navigation parameter error is reduced before filtering. Yadav et al. [29] clarifies about the advancement of GPS and INS models and demonstrate in getting the exact values in all aspects. Zhou et al. [30], Derbel et al. [31], Oh and Hwang [32], Chen [33], Choi et al. [34], Liu et al. [35] has improved the integrated navigation method to varying degrees. The particle swarm optimization (PSO) has received increased attention in many research fields in recent years [36]. PSO was first proposed by Eberhart and Kennedy [37]. PSO is a simple and effective optimization algorithm that can achieve fast convergence by adjusting parameters [38–40]. Cai et al. [41], Li et al. [42], Liu [43], Qu et al. [44] have developed a variety of applications and developments in PSO. This paper is dedicated to promoting the application of LiDAR remote sensing methods in agriculture and canal irrigation is the top priority of agricultural production. The ecological irrigation canal is the main content of the construction of water-saving and ecological irrigation areas, which is an important link in the process of building modern agriculture. The water canal was built in the 1950s for irrigation to maintain local agriculture during the dry season [45]. The construction of ecological irrigation canals plays an important role in improving the water environment and alleviating the shortage of water resources. Therefore, the construction of ecological irrigation canals is the only way for the development of China's agricultural modernization. Agricultural water use efficiency has been affected by farming methods, fertilization methods, and irrigation schedules, which is also affected by the construction of farmland water conservancy infrastructure [46–48]. Because of the unstable precipitation in arid and semi-arid regions, irrigation channels are important for food and food supplies in these areas [49,50]. From the aspect of technical efficiency, the efficiency of water allocation can be improved through water circulation and irrigation [51,52]. Therefore, the construction of ecological irrigation canals is the only way for the development of China's agricultural modernization. At the same time, the efficiency of agricultural water can be increased.

The aim of this paper is to develop and apply an approach that realizes the extraction of ecological irrigation areas and the establishment of a three-digit model of ground crops. Through these efforts, we will lay the foundation for the establishment of a three-dimensional digital model of ecological irrigation channels and crops in the future and thereby promote the digitization of agricultural production. The other sections are arranged as follows: section 2 – Global Navigation Satellite System/Inertial Navigation System (GNSS/INS) integrated navigation system model is built, the PSO algorithm was introduced; In section 3, Point cloud data acquisition was introduced; section 4, the feature extraction algorithm was introduced; section 5 is experiment and verification, the validity of the PSO algorithm is verified and the model of ecological irrigation canal and three ground groups were established, the reasons for the test error are also discussed in detail.

2. GNSS/INS integrated navigation system

2.1. GNSS and INS error model

The coordinate system of INS adopts the "geographical coordinates of East-North-Up (ENU)". The navigation information error is nine-dimensional, including the three-dimensional platform error angle φ_E, φ_N, φ_U, the three-dimensional

speed error $\delta\dot{v}_E, \delta\dot{v}_N, \delta\dot{v}_U$ and the three-dimensional position error $\delta\lambda$, δL, δh. The earth's rotation angular velocity is w_{ie}, The ellipsoidal equatorial plane radius R_e = 6,370,000 m, radius of curvature in prime vertical $R_N = R_e(1 + f\sin^2 L)$, radius of meridional section $R_M = R_e(1 - 2f + 3f\sin^2 L)$. Ovality is f = 1/298.257, the velocities along the ENU direction are v_E, v_N, v_U, the longitude, latitude, and altitude are λ, L, h; equivalent gyro drifts in ENU directions are ε_E, ε_N, ε_U, the equivalent accelerometer error is $\nabla_E, \nabla_N, \nabla_U$.

- *Speed error equation*:

$$\delta\dot{v} = f^n \times \varphi^n - \left(2\delta\omega_{ie}^n + \delta\omega_{en}^n\right) \times v^n - \left(2\omega_{ie}^n + \omega_{en}^n\right) \times \delta v^n + \nabla^n \quad (1)$$

- *Platform error angle equation*:

$$\dot{\varphi}^n = \delta\omega_{ie}^n + \delta\omega_{en}^n - \left(\omega_{ie}^n + \omega_{en}^n\right) \times \varphi^n + \varepsilon^n \quad (2)$$

- *Position error equation*:
  According,

$$\dot{L} = \frac{v_N}{R_N + h}, \dot{\lambda} = \frac{v_E \sec L}{R_N + h}, \dot{h} = V_U \quad (3)$$

The position error equation is obtained as follow:

$$\begin{cases} \delta\dot{L} = -\dfrac{\delta v_N}{R_M + h} \\ \delta\dot{\lambda} = -\dfrac{\delta v_E}{R_N + h}\sec L + \dfrac{v_E}{R_N + h}\delta L \sec L \tan L \\ \delta\dot{h} = \delta v_U \end{cases} \quad (4)$$

With GPS as the representative, the GNSS error model is deduced as follow:

$$\dot{X}_G = A_G X_G + D_G \xi_G \quad (5)$$

Because the carrier is stationary, in the GPS receiver data acquisition interval, the speed as a constant value, so only consider the horizontal direction. The error model of GPS selects four-dimensional state model:

$$X_G = \left[\sigma v_{Gn}, \sigma v_{Ge}, \sigma L_G, \sigma\lambda_G\right]^T \quad (6)$$

$$A_G = \begin{bmatrix} 0 & 0 & 0 & 0 \\ 0 & 0 & 0 & 0 \\ \dfrac{1}{R_M + h} & 0 & 0 & 0 \\ 0 & 0 & 0 & 0 \end{bmatrix} \quad (7)$$

where the earth radius is $R_M = R_e(1 - 2f + 3f\sin^2 L)$, $R_N = R_e(1 + f\sin^2 L)$, f = 1/298.257.

2.2. GNSS/INS integrated navigation system model

The corresponding equation of state is given by

$$\hat{X} = FX + Gw \quad (8)$$

where $X = [X_I, X_G]^T$ is state variable, $F = \begin{bmatrix} F_I & 0 \\ 0 & F_G \end{bmatrix}$ is state transition matrix, $G = \begin{bmatrix} G_I & 0 \\ 0 & G_G \end{bmatrix}$ is dynamic noise matrix, $w = [w_I, w_G]^T$ is the process white noise matrix of the system, the subscript "I" and "G" represent INS and GNSS.

In this paper, the speed difference and the position difference are chosen as the external observations to establish the combined measuring equations of position and velocity.

$$\begin{bmatrix} L_{\text{INS}} \\ \lambda_{\text{INS}} \\ h_{\text{INS}} \end{bmatrix} = \begin{bmatrix} L_t + \delta L \\ \lambda_t + \delta\lambda \\ h_t + \delta h \end{bmatrix} \quad (9)$$

where L_{INS}, λ_{INS} and h_{INS} represent the longitude, latitude and altitude calculated by the INS L_t, λ_t, h_t, represent the carrier's true longitude, latitude and altitude information, δL, $\delta\lambda$, δh represent the longitude error, latitude error and height error solved by INS.

$$\begin{bmatrix} L_{\text{GPS}} \\ \lambda_{\text{GPS}} \\ h_{\text{GPS}} \end{bmatrix} = \begin{bmatrix} L_t - \dfrac{N_n}{R} \\ \lambda_t - \dfrac{N_e}{R\cos L} \\ h_t - N_u \end{bmatrix} \quad (10)$$

where N_n, N_e, N_u represent position error of GNSS receiver along the direction of ENU. Then the external measurement position error can be defined as $Z_{\text{pos}} = L_{\text{INS}} - L_{\text{GPS}}$. The location measurement equation is given by:

$$Z_{\text{POS}} = H_{\text{POS}}(t)X(t) + V_{\text{POS}}(t) \quad (11)$$

GPS and INS speed measurement information are shown as follows:

$$\begin{bmatrix} v_{e\text{INS}} \\ v_{n\text{INS}} \\ v_{u\text{INS}} \end{bmatrix} = \begin{bmatrix} v_e + \delta v_e \\ v_n + \delta v_n \\ v_u + \delta v_u \end{bmatrix} \quad (12)$$

where v_e, v_n, v_u represent the speed along with the direction of ENU solved by INS; v_e, v_n, v_u are the true speed along with the direction of ENU under the geographic coordinate system, δv_e, δv_n, δv_u represent the speed error along with the direction of ENU solved by INS.

$$\begin{bmatrix} \nu_{e\mathrm{GPS}} \\ \nu_{n\mathrm{GPS}} \\ \nu_{u\mathrm{GPS}} \end{bmatrix} = \begin{bmatrix} \nu_e - M_e \\ \nu_n - M_n \\ \nu_u - M_u \end{bmatrix} \tag{13}$$

where M_e, M_n, M_u are the components of the velocity measurement errors on the three axes of East-North-Up. The velocity error of the external measurement can be defined as $Z_{\mathrm{vel}} = \begin{bmatrix} \nu_{e\mathrm{INS}} - \nu_{e\mathrm{GPS}} \\ \nu_{n\mathrm{INS}} - \nu_{n\mathrm{GPS}} \\ \nu_{u\mathrm{INS}} - \nu_{u\mathrm{GPS}} \end{bmatrix}$. The velocity measurement equation is given by:

$$Z_{\mathrm{vel}} = H_{\mathrm{vel}}(t)X(t) + V_{\mathrm{vel}}(t) \tag{14}$$

According to Eqs. (9)–(14), we can get a GNSS/INS integrated navigation system's position and velocity combination measurement equation:

$$Z(t) = \begin{bmatrix} \lambda_{\mathrm{INS}} - \lambda_{\mathrm{GPS}} \\ L_{\mathrm{INS}} - L_{\mathrm{INS}} \\ h_{\mathrm{INS}} - h_{\mathrm{INS}} \\ \nu_{e\mathrm{INS}} - \nu_{e\mathrm{GPS}} \\ \nu_{n\mathrm{INS}} - \nu_{n\mathrm{GPS}} \\ \nu_{u\mathrm{INS}} - \nu_{u\mathrm{INS}} \end{bmatrix} = H(t)X(t) + V(t) \tag{15}$$

2.3. GNSS/INS integrated navigation information fusion framework

In this paper, centralized Kalman filtering is used to process INS and GNSS data. INS and GNSS data are sent to the same Kalman filter. When the state vector in the filtering equation is a combination of the error state of the INS navigation parameter and the error state of the GPS navigation parameter as follow:

$$\Delta X = \Delta X_I + \Delta X_G \tag{16}$$

Then the Kalman filter's optimal error estimation $\left(\Delta\hat{X}_I, \Delta\hat{X}_G\right)$ can correct the original system to obtain accurate navigation parameters. In this paper, the discrete Kalman filter algorithm is introduced to estimate the state estimation of the next moment according to the system state estimation of the previous moment through the recursive algorithm. The system does not need to store a large amount of measured data. The estimation process is shown by the following five equations:

- *State one-step prediction*:

$$\hat{X}_{(k/k-1)} = \Phi_{k,k-1}\hat{X}_{k-1} \tag{17}$$

- *Predict the mean square error*:

$$P_{(k/k-1)} = \Phi_{k,k-1}P_{k-1}\Phi_{k,k-1} + \Gamma_{k-1}Q_{k-1}\Gamma_{k-1}^T \tag{18}$$

- *Filter gain*:

$$K_k = P_{(k/k-1)}H_k^T\left(H_kP_{(k/k-1)}H_k^T + R_k\right)^{-1} \tag{19}$$

- *Optimal state estimation*:

$$\hat{X}_k = \hat{X}_{(k/k-1)} + K_K\left(Z_K - H_K\hat{X}_{(k/k-1)}\right) \tag{20}$$

- *Estimate the mean square error*:

$$P_k = \left(I - K_kH_k\right)P_{(k/k-1)} \tag{21}$$

where Q is system noise covariance matrix, R is measurement noise covariance matrix, $\Phi_{k,k-1}$ is the one-step transfer matrix from the time instant t_{k-1} to time instant t_k, Γ_{k-1} is system noise driver array; H_k is measurement array, V_k is measurement noise sequence. Given the initial value $\hat{X}_0$ and P_0, according to the k moment of measurement Z_k, the state estimations X_k (k = 1, 2, 3…) can be recursive calculated by the measurement Z_k of the kth moment.

2.4. PSO algorithm

Assume that in the D-dimensional search space, a population of n particles $X = (X_1, X_2, \ldots, X_n)$, where the i-th particle is represented as a D-dimensional vector $X_i = (X_{i1}, X_{i2}, \ldots, X_{iD})^T$, representing the position of the i-th particle in the D-dimensional search space and a potential solution to the problem. According to the objective function, the fitness value corresponding to each particle position X_i can be calculated. The velocity of the i-th particle is $V_i = (V_{i1}, V_{i2}, \ldots V_{iD})$, the individual extremum is $P_i = (P_{i1}, P_{i2}, \ldots, P_{iD})^T$ and the population extremum of the population is $P_g = (P_{g1}, P_{g2}, \ldots, P_{gD})^T$. During each iteration, the particles update their speed and position through individual extremum and population extremum. The formula is as follows:

$$V_{ij}(t+1) = wV_{ij}(t) + c_1r_1\left[P\mathrm{best} - x_{ij}(t)\right] + c_2r_2\left[G\mathrm{best} - x_{ij}(t)\right] \tag{22}$$

$$x_{ij}(t+1) = x_{ij}(t) + V_{ij}(t+1) \tag{23}$$

where V_{ij} and x_{ij} are the velocity and position of particle i in the j-th dimension respectively; P best is the individual optimal position of the space search after particle i traversal; Gbest is the global optimal position of all particles searched so far; t represents the current time; c_1 and c_2 are non-negative constants called acceleration factors; r_1 and r_2 are random numbers distributed in the interval (0,1).

In this paper, the fitness function is as follow:

$$S = V\mathrm{ar}(X_{\mathrm{Lo}}) + V\mathrm{ar}(X_{\mathrm{La}}) + V\mathrm{ar}(X_{\mathrm{Ev}}) + V\mathrm{ar}(X_{\mathrm{Nv}}) \tag{24}$$

where X_{Lo} is the longitude error, X_{La} is the latitude error, X_{Ev} is the eastward velocity error, X_{Nv} is the northward velocity error.

3. Point cloud data obtain and processing

Establishing accurate models of ground objects can play an important role in urban design planning, agricultural

production, and water conservancy construction. The modeling process of low-altitude remote sensing, oblique photogrammetry, and LiDAR-based 3D modeling is given in Fig. 1.

All three methods can generate three-dimensional models of targets, but methods (a) and (b) use passive sensing devices to obtain image data, which is greatly affected by the intensity of light. The LiDAR used in the method (c) belongs to the active remote sensing device, which can still work normally under the meteorological conditions and nighttime when the light is weak. In addition, multi-image matching is a key step in the method (a) and (b) operation. The goal of establishing a three-dimensional model in this paper is mainly for crops and irrigation canals in ecological irrigation districts. The modeling results of methods (a) and (b) are severely affected when the model object is a large area of wheat. Because the background color is all green, the matching of the correspondence points will cause a large error due to the inability to find an obvious reference. In addition, the problem of precision control needs to be considered, and methods (a) and (b) do not perform well in the measurement of elevation accuracy, so more production time and cost are required in order to improve the elevation precision. Method (c) can directly generate a target point cloud with no requirements for the color and background of the target. It reduces the requirements of the operating environment and saves a lot of production time.

3.1. Coordinate transformation

After obtain calculating the distance R between the laser transmitting point and the target point, it is necessary to obtain the three-dimensional space coordinates in the World Geodetic System-1984 Coordinate System (WGS-84) through the transformation of multiple coordinate systems. Therefore, in the laser beam coordinate system, the laser foot point can be expressed as:

$$\begin{bmatrix} x_{\mathrm{LP}} \\ y_{\mathrm{LP}} \\ z_{\mathrm{LP}} \end{bmatrix} = \begin{bmatrix} 0 \\ 0 \\ R \end{bmatrix} \tag{25}$$

In the laser scanning coordinate system, the laser foot point can be expressed as:

$$\begin{bmatrix} x_P \\ y_P \\ z_P \end{bmatrix} = \begin{bmatrix} 1 & 0 & 0 \\ 0 & \cos\theta_i & -\sin\theta_i \\ 0 & \sin\theta_i & \cos\theta_i \end{bmatrix} . \begin{bmatrix} 0 \\ 0 \\ R \end{bmatrix} \tag{26}$$

where θ_i is the instantaneous scanning angle of the laser beam, which is mainly calculated by the number of system scanning angle θ and system scanning angle *N*, then the calculation formula of the number of *i* instantaneous scanning angle is:

$$\theta_i = \frac{\theta}{2} - i \times \frac{\theta}{N-1} \tag{27}$$

In the airborne LiDAR system, the scanning device and INS of LiDAR must have certain angle errors in installation, so their coordinate systems can't be guaranteed to be parallel. We suppose that the angle between the two coordinate systems and the three coordinate axes is α, β, γ and the offset between the origin of the two coordinates is $(\Delta x_L, \Delta y_L, \Delta z_L)^T$. Therefore, the laser foot point is expressed in the inertial navigation platform coordinate system as follows:

$$\begin{bmatrix} X_I \\ y_I \\ z_I \end{bmatrix} = R_I \times \begin{bmatrix} x_p \\ x_p \\ x_p \end{bmatrix} + \begin{bmatrix} \Delta x_L \\ \Delta y_L \\ \Delta z_L \end{bmatrix} \tag{28}$$

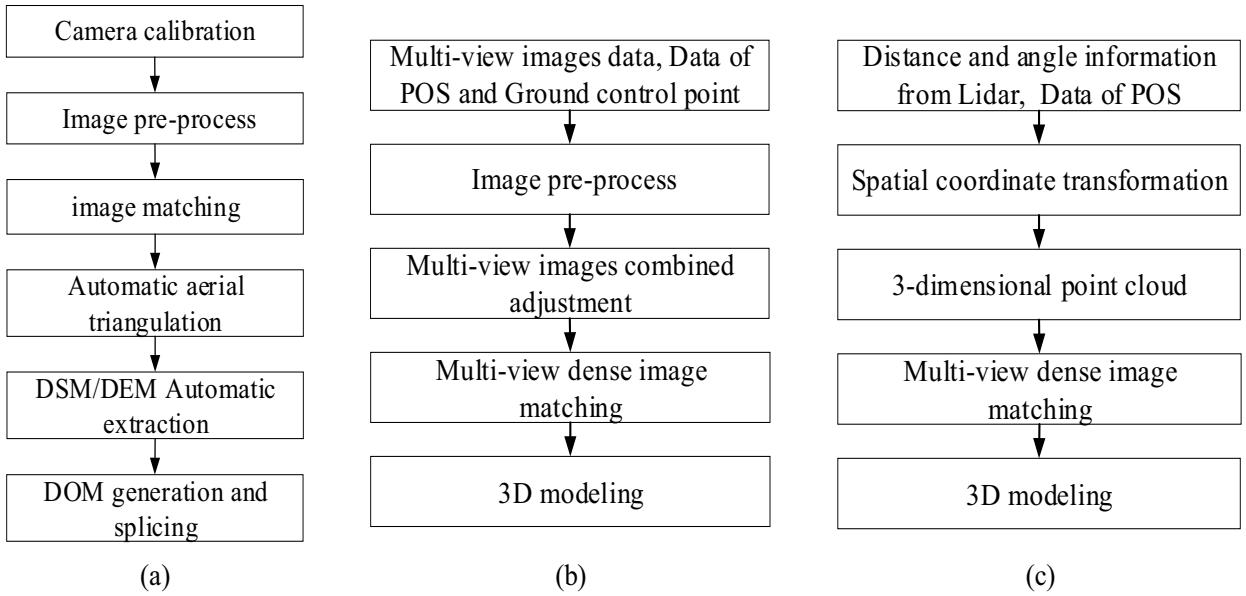

Fig. 1. (a) Low-altitude remote sensing, (b) oblique photogrammetry, and (c) LiDAR-based 3D modelling.

where R_I is the transformation matrix, among them:

$$R(\alpha)=\begin{bmatrix}1 & 0 & 0\\ 0 & \cos\alpha & -\sin\alpha\\ 0 & \sin\alpha & \cos\alpha\end{bmatrix},\ R(\beta)=\begin{bmatrix}\cos\beta & 0 & \sin\beta\\ 0 & 1 & 0\\ -\sin\beta & 0 & \cos\beta\end{bmatrix}$$

$$R(\gamma)=\begin{bmatrix}\cos\gamma & -\sin\alpha & 0\\ \sin\gamma & \cos\gamma & 0\\ 0 & 0 & 1\end{bmatrix}$$

There is an eccentricity $(\Delta x_I, \Delta y_I, \Delta z_I)^T$ between the phase center of GPS and the reference center of the inertial navigation platform. The Inertial Measurement Unit (IMU) can measure the roll angle, pitch angle and yaw angle, respectively as ϕ, φ, ψ, according to these three Rotating Euler angles, the conversion from the inertial platform to the local coordinate system can be realized. The laser foot point is expressed in the local coordinate system $(x_{\mathrm{LH}}, y_{\mathrm{LH}}, z_{\mathrm{LH}})^T$ as:

$$\begin{bmatrix}x_{\mathrm{LH}}\\ y_{\mathrm{LH}}\\ z_{\mathrm{LH}}\end{bmatrix}=R_B\cdot\begin{bmatrix}x_I\\ y_I\\ z_I\end{bmatrix}-R_B\cdot\begin{bmatrix}\Delta x_I\\ \Delta y_I\\ \Delta z_I\end{bmatrix} \tag{29}$$

where $R_B = R(\phi)R(\varphi)R(\psi)$ is the transformation matrix, among them: $R(\phi)=\begin{bmatrix}1 & 0 & 0\\ 0 & \cos\phi & -\sin\phi\\ 0 & \sin\phi & \cos\phi\end{bmatrix}$.

$$R(\varphi)=\begin{bmatrix}\cos\varphi & 0 & \sin\varphi\\ 0 & 1 & 0\\ -\sin\varphi & 0 & \cos\varphi\end{bmatrix},\ R(\psi)=\begin{bmatrix}\cos\psi & -\sin\psi & 0\\ \sin\psi & \cos\psi & 0\\ 0 & 0 & 1\end{bmatrix}$$

After obtaining the coordinates of the laser foot point in the local horizontal coordinate system, the coordinates in the WGS-84 coordinate system $(x_{w84}, x_{w84}, x_{w84})^T$ can be obtained through the coordinate transformation again:

$$\begin{bmatrix}x_{w84}\\ y_{w84}\\ z_{w84}\end{bmatrix}=R_W\cdot R_G\cdot\begin{bmatrix}x_{\mathrm{LH}}\\ y_{\mathrm{LH}}\\ z_{\mathrm{LH}}\end{bmatrix}+\begin{bmatrix}x_{84}\\ y_{84}\\ z_{84}\end{bmatrix} \tag{30}$$

where R_W is the rotation function associated with latitude and longitude, R_G is the coordinate rotation matrix due to vertical misalignment and the coordinate of the antenna phase center of GPS system in the WGS-84 coordinate system is $(x_{84}, y_{84}, z_{84})^T$. According to Eqs. (25)–(30), the 3D spatial coordinate of the target point is:

$$\begin{bmatrix}x_{w84}\\ y_{w84}\\ z_{w84}\end{bmatrix}=R_W\cdot R_G\cdot R_B\cdot\left(R_I\cdot R_L\cdot\begin{bmatrix}0\\ 0\\ R\end{bmatrix}+\begin{bmatrix}\Delta x_L\\ \Delta y_L\\ \Delta z_L\end{bmatrix}-\begin{bmatrix}\Delta x_I\\ \Delta y_I\\ \Delta z_I\end{bmatrix}\right)+\begin{bmatrix}x_{84}\\ y_{84}\\ z_{84}\end{bmatrix} \tag{31}$$

where $R_L=\begin{bmatrix}1 & 0 & 0\\ 0 & \cos\theta_i & -\sin\theta_i\\ 0 & \sin\theta_i & \cos\theta_i\end{bmatrix}$ is the transformation matrix.

3.2. Point cloud data processing

After obtaining the three-dimensional point cloud data of the ecological irrigation canal and surrounding areas with UAV, the point cloud data of other objects unrelated to the ecological irrigation canal, such as buildings and cars, must be removed.

In order to simplify the data structure and improve computational efficiency, we adopt the method of virtual grid handling processing first point cloud data. To a certain extent, the error caused by the interpolation of a regular lattice net is reduced. It's also structurally quite simple. The position of each point can be calculated by the following formula:

$$\begin{cases}X_{\mathrm{id}}=\dfrac{X_k-X_{\min}}{\mathrm{cellsize}}\\ Y_{\mathrm{id}}=\dfrac{Y_k-Y_{\min}}{\mathrm{cellsize}}\end{cases} \tag{32}$$

where X_k, Y_k are the coordinates of a point, $X_{\min}$, $Y_{\min}$ is the minimum in the X, Y direction, cell size is the edge length of the partition grid.

Mathematical morphological filtering methods include open and close operations, the two algorithms are composed of basic operations of expansion and corrosion. When processing point cloud data, the maximum elevation value of point cloud in the filtering window will be selected as the new elevation value of the point. The formula is as follows:

$$\left[\delta_B(f)\right](x,y)=\max\left\{\begin{matrix}f(x+i,y+j)\mid i,\\ j\in\left[-w,w\right];(x+i),(y+i)\in D_f\end{matrix}\right\} \tag{33}$$

The corrosion operation is to select the minimum elevation value of the point cloud in the filtering window as the new elevation value of the point. The formula is as follows:

$$\left[\varepsilon_B(f)\right](x,y)=\min\left\{\begin{matrix}f(x+i,y+j)\mid i,\\ j\in\left[-w,w\right];(x+i),(y+i)\in D_f\end{matrix}\right\} \tag{34}$$

The first operation is corrosion and then expansion. The closed operation is opposite, the formula is as follows:

$$\begin{cases}\gamma_B(f)=\delta_B\left[\varepsilon_B(f)\right]\\ \beta_B(f)=\varepsilon_B\left[\delta_B(f)\right]\end{cases} \tag{35}$$

The method of opening operation is generally used to acquire 3D point cloud data on the ground, that is, to remove the non-ground 3D point cloud data. Using Eq. (36) to calculate the difference between the elevation value of the original point cloud data and the elevation value after opening operation and then compare the difference with the

filtering threshold T. If it is greater than T, remove the point, otherwise remain.

$$dH = f - \delta_B\left[\varepsilon_B(f)\right] \tag{36}$$

The flow chart of point cloud data processing in the target area is shown in Fig. 2.

4. Feature extraction

After obtaining the point cloud data of the ecological irrigation canal area, it is necessary to extract its characteristic lines. The method of extracting the characteristic line of the point cloud of the building is suitable for the extraction of the intersection line of the surface and the surface. The same characteristic line exists in the ecological irrigation canal. Therefore, the point cloud data of the ecological irrigation canal area are processed in section 3. The k-dimensional (K-D) tree [53] is used to search the local K-neighborhood of point $Np_i = \left\{(x_j, y_j, z_j) \in R^3 \mid j = 1,2,3\ldots k\right\}$ and find out the Euclidean distance of current point P_i, and it can be shown as follow:

$$\text{dist} = \sqrt{(x_i - x_j)^2 + (y_i - y_j)^2 + (z_i - z_j)^2} \mid (x_j, y_j, z_j) \in Np_i \tag{37}$$

Sort the selected k points by distance from large to small and take the current point as a vertex. As shown in Fig. 3, the three-neighborhood points A, B, C constitute a plane triangle. Calculate the distance from p_i to triangle ABC. The point d_j on the characteristic line is larger, the point d_j on the ground and slope is smaller. In order to reduce the noise influence on the extraction of characteristic line, the average value of d_j is compared to the set threshold $d_{\min}$, if the average value $\bar{d}$ is greater than the set threshold, then the point remains.

Most sections of ecological irrigation canals are inverted trapezoidal or rectangular. Taking the inverted trapezoidal section as an example, the characteristic line schematic diagram is shown in Fig. 4.

However, unlike the extraction of the characteristic lines of a building, the ecological irrigation canal is rougher than the wall surface of the building and there is an influence of debris such as stones and weeds.

Therefore, the set threshold must be accurate, otherwise, it will cause a greater error. In this paper, the first calculation of the ecological irrigation canal characteristics line is the ecological irrigation area slope d_j, then take the average $\bar{d}_1$ as the set threshold $d_{\min}$ and compare with $\bar{d}$. This way avoids deleting points on the true feature line because the selected $d_{\min}$ is small when the surface of the ecological irrigation canal slope is rough and there is a lot of debris.

5. Experiment and verification

5.1. PSO experiment

We use a joint optimization method for the system noise variance matrix Q and the measurement noise matrix R. When performing the PSO algorithm, we set the number of iterations to 30, 50, and 100 times. There are 12 parameters for optimizing Q and R, and the range of values we set in this paper is as follows: The upper limit of the values of and is 0.01, 0.01, 0.01, 0.01, 0.01, 0.01, 0.05, 0.05, 0.05, 0.05, 0.05, and 0.05. The lower limit of the values of and is 0.00001, 0.00001, 0.00001, 0.0025, 0.0025, 0.002, 0.0001, 0.001, 0.0001, 0.2, 0.2, and 0.

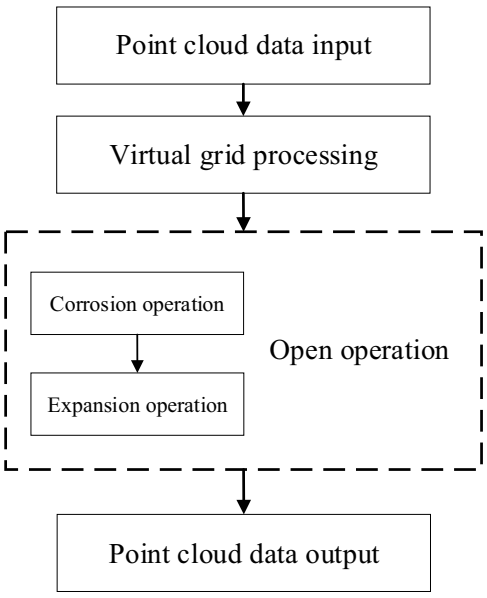

Fig. 2. Point cloud data processing.

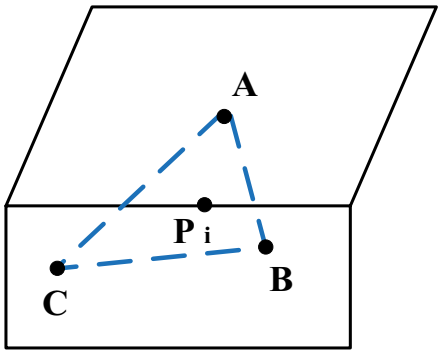

Fig. 3. Feature point and plane triangle schematic.

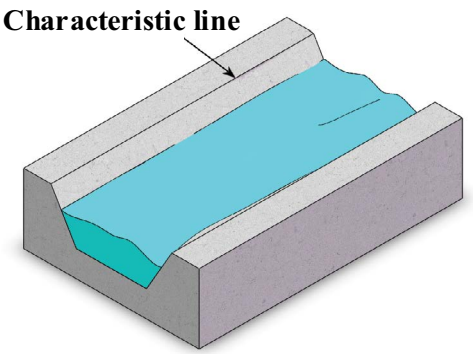

Fig. 4. Ecological irrigation canal section and characteristic line.

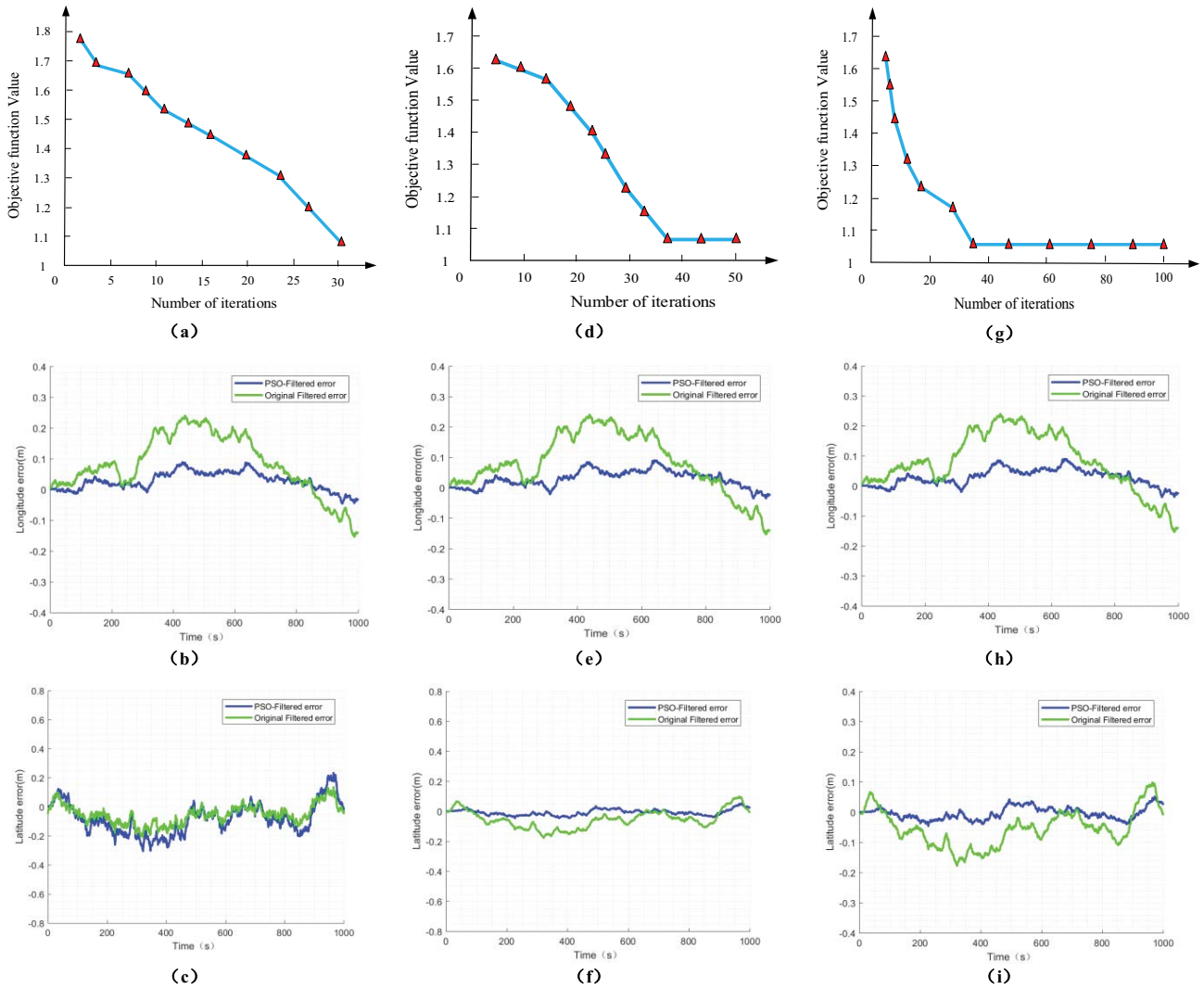

Fig. 5. Objective function value curve; latitude and longitude error curve.

When the number of iterations is 30, 50, and 100 times, the iteration convergence curve, longitude, and latitude error curve are shown in Fig. 5. Figs. 5a–c and Table 1 show that the error parameters of longitude and latitude are greatly reduced when the number of iterations is 30 times. The variance of PSO-filtered error of longitude error is 0.00086, the variance of PSO-filtered error of latitude error is 0.00059, the optimal objective function value is 1.0614. But the iterative convergence curve shows that the number of iterations is 30 times, the curve does not completely converge, so the number of iterations must be increased. When the number of iterations is 50 times, Figs. 5d–f and Table 1 show that the error of the latitude and longitude error phase is further reduced. The variance of PSO-Filtered error of Longitude error is 0.00077, the variance of PSO-filtered error of latitude error is 0.0004, the optimal objective function value is 0.84712. The convergence characteristic curve has converged, but to prevent the optimization from falling into local optimum, the number of iterations is increased to 100 times. Figs. 5g–i and Table 1 show that the number of iterations is 100 times, the variance of PSO-filtered error of longitude error is 0.00076, the variance of PSO-filtered error of latitude error is 0.00041, the optimal objective function value is: 0.84906. The above chart shows that after the optimization curve enters the global optimum at the 38th iteration, the iteration still converges at the same position when the number of iterations is 100, and the longitude error and the latitude error have no significant change compared with 50 times, which indicates that the optimization result is the optimal state.

5.2. 3D model generation of ground crops

In order to verify the effectiveness of this algorithm, as shown in Fig. 6, we use RPLIDAR A2 and fix it on the UAV to collect data, the GPS module and the IMU are also installed. The parameters of the Lidar are shown in Table 2.

The data output from LiDAR system includes Chiptime, $a_z(g)$, $a_y(g)$, $a_z(g)$, w_x(deg/S), w_y(deg/S), w_z(deg/S), angle$_x$(deg), angle$_y$(deg), angle$_z$(deg), Lon(deg), Lat(deg). Herein,

Chiptime is the timestamp corresponding to the collected data. $a_x(g)$, $a_y(g)$, $a_z(g)$ is the acceleration of the current carrier along each of the three axes. w_x(deg/S), w_y(deg/S), w_z(deg/S) is the angular velocity of the three axes of the current carrier. Angle$_x$(deg), angle$_y$(deg), angle$_z$(deg) is the roll, pitch and yaw attitude angle. Lon(deg), Lat(deg) is longitude and latitude. Airborne LiDAR system can collect point cloud data and longitude and latitude information at the same time. We selected three representative ground crops in the agricultural irrigation area as the target of this experiment.

Wheat represents the most widely grown food crop, and *Euonymus japonicus* and *Anemone* have both medicinal value and ornamental value. The three ground groups are shown in Figs. 7a, c, e and g. The three-dimensional digital model is shown in Figs. 6b, d, f and h.

The experiments are run on the MATLAB 2017 (a) platform. As shown in Fig. 7, the direction of the red arrow is the direction of the UAV flight. The height of UAV from the ground target is set at 5 m. According to the point cloud data obtained in section 3, we obtained point cloud data for the target crop. MATLAB is used to build a three-dimensional digital model of the target crop. As shown in Fig. 7, the 3D model of the wheat, *Euonymus japonicus* and *Anemone* were built. The error between the 3D model and the actual crop average height data is compared in Table 3. In order to detect the accuracy of generating a three-dimensional model, the average height of each ground crop is calculated by taking a certain number of sampling points on the surface of the crop. As shown in Table 3, the average height of wheat is 712.63 and 526.306 mm, the 3D model average height of wheat is 678.58 and 502.832 mm, the average height of *Euonymus japonicus* is 920.33 mm, the 3D model average height of the sedum *Euonymus japonicus* is 867.65 mm. The average height of the *Anemone* is 410 mm, the 3D model average height of the *Anemone* is 440 mm.

5.3. Ecological irrigation canal extraction

In order to verify the extraction method of the ecological irrigation canal characteristic line proposed in this paper, we also selected an ecological irrigation canal for data collection in the Hetao irrigation area of Inner Mongolia. The ecological irrigation canal and the three-dimensional digital model of the ecological irrigation canal are shown in Fig. 8 at different angles and the characteristic lines are obvious.

As shown in Table 4, the errors between the actual value and the 3D model in average depth and height are 4.42% and

Table 2
LiDAR parameters

Name	RPLIDAR A2
Line number	Single
Weight	190 g
Effective distance	18 m
Precision	+/–4 cm
Scanning frequency	5–15 HZ

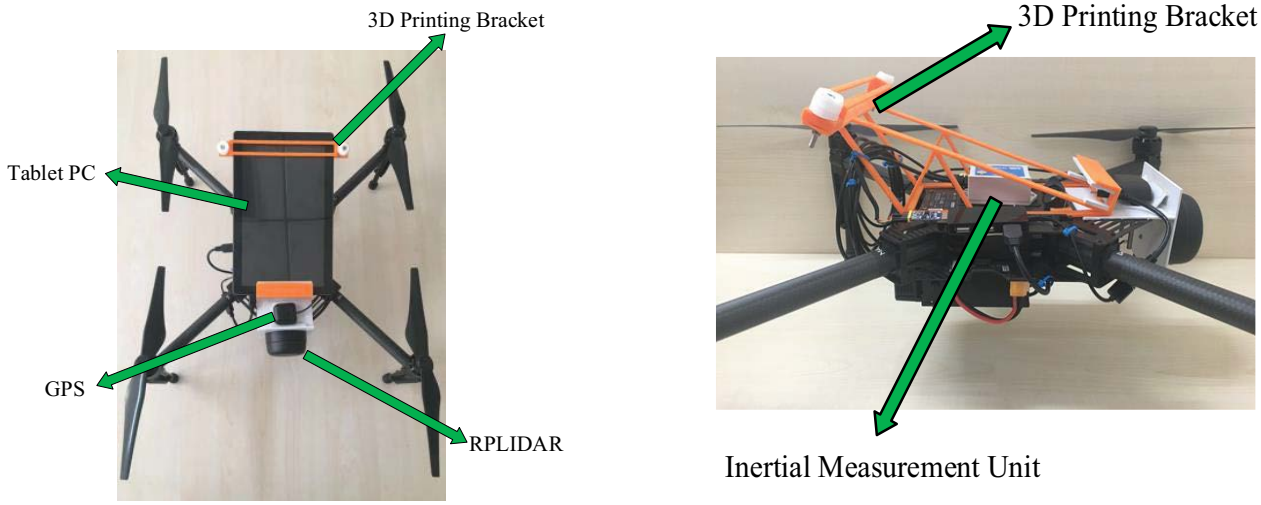

Fig. 6. Airborne LiDAR remote sensing system.

Table 1
Navigation parameters variance

	30 iterations		50 iterations		100 iterations	
Navigation parameters	Longitude	Latitude	Longitude	Latitude	Longitude	Latitude
Variance of original filtered error	0.0091	0.0047	0.0091	0.0047	0.0091	0.0047
Variance of PSO-filtered error	0.00086	0.00059	0.00077	0.0004	0.00076	0.00041

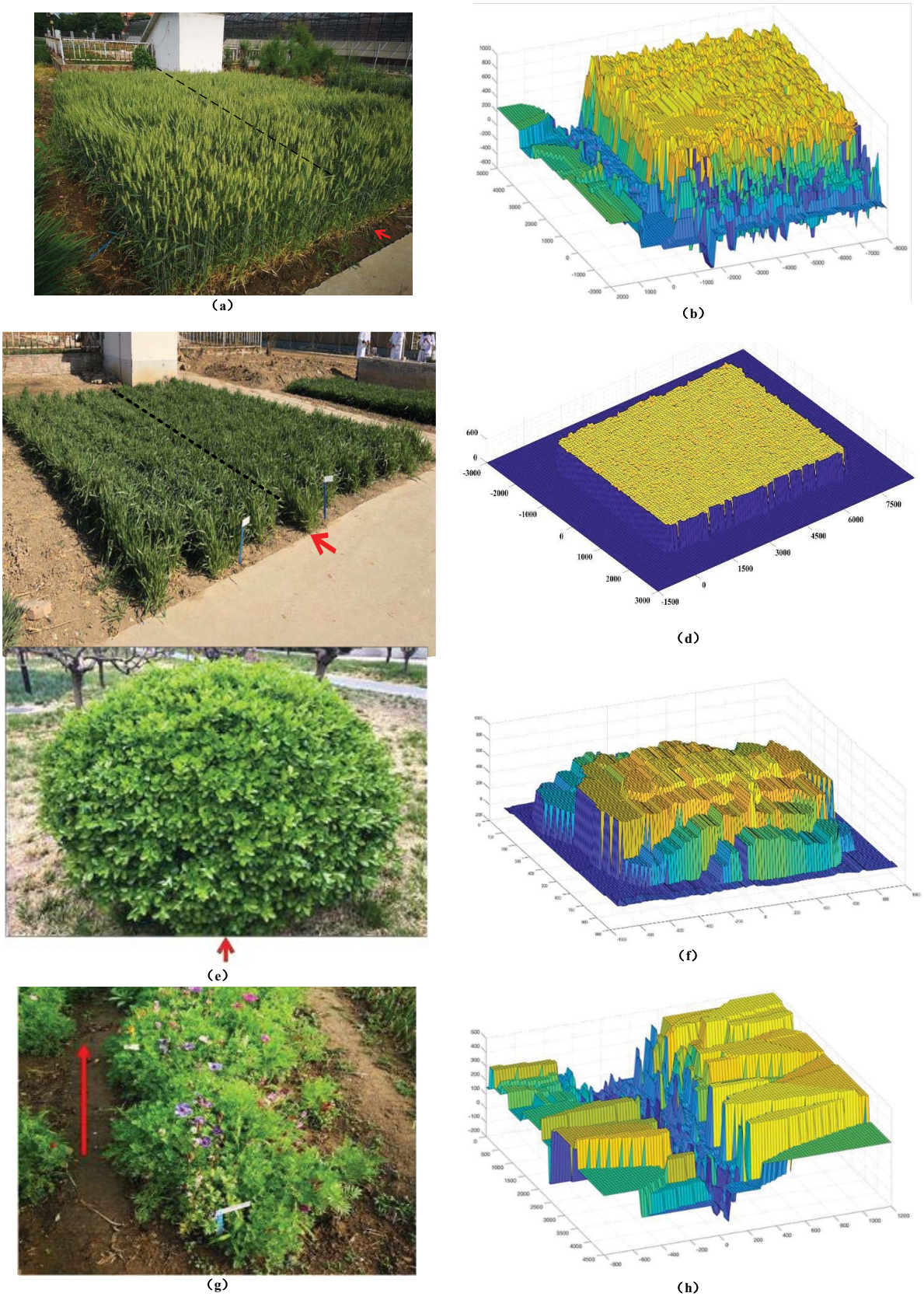

Fig. 7. The ground group (a) wheat in grouting period, (b) wheat in the jointing stage, (c) *Euonymus japonicus*, (g) *Anemone*, (b, d, f and h) are three-dimensional digital models corresponding to ground crops.

Table 3
3D model and actual crop average height data comparison

Crop	$Wheat_{(a)}$	$Wheat_{(c)}$	*Euonymus japonicus*	*Anemone*
Actual crop average height	712.63	526.306	920.33	410
3D model average height	678.58	502.832	867.65	440
Error	4.78%	4.46%	5.72%	7.31%

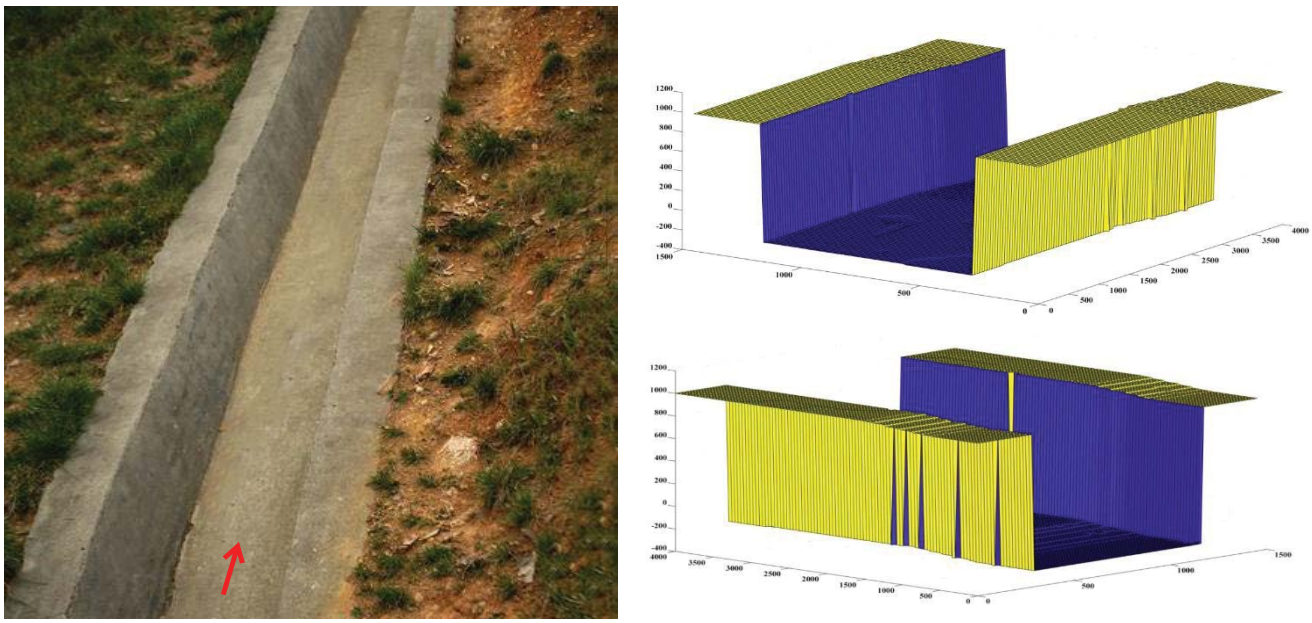

Fig. 8. Ecological irrigation canal.

4.56%. The 3D model can reflect the shape and size of real ecological irrigation canals. The experiment proves that the airborne LiDAR point cloud data acquisition system works well. The ecological irrigation canal extraction algorithm proposed in this article is effective.

5.4. Discussion

In this section, a LiDAR remote sensing data acquisition system based on light multi-rotor UAV is established to collect point cloud data of ground targets. The linear decreasing PSO experiments, three-dimensional digital model generation of ground crops and extraction of ecological irrigation canals are carried out separately. The method of MATLAB simulation is used to verify that the Kalman filtering algorithm optimized by linear decreasing PSO can reduce the positioning error of the integrated navigation system. The three-dimensional digital model of surface crops and ecological irrigation canals are established. The error between the actual target and 3D model mainly comes from the following two aspects after analysis: (1) LiDAR ranging error, the LiDAR used in this paper has an error is +/–4 cm at the distance of 10 meters. (2) The mounting position error between the LiDAR and the inertial navigation sensor is preserved with the matrix transformation of the point cloud data.

Table 4
3D model and actual value data comparison of irrigation canal

	Average depth	Average width
Actual value	1,200 mm	900 mm
3D model value	1,253 mm	859 mm
Error	4.42%	4.56%

6. Conclusions

Further increasing the application of advanced sensors such as LiDAR in agricultural production meets the requirements of current digital agricultural development. In traditional mapping operations, the camera is heavily influenced by weather and lighting factors, which greatly increases the difficulty of post-processing. The remote sensing methods of fixed-wing aircraft and satellite-equipped LiDAR are costly and have low real-time performance. The linear descending PSO algorithm is used to improve the positioning accuracy of multi-rotor UAV remote sensing. Experiments show that the linear decreasing PSO algorithm can greatly improve the latitude and longitude output accuracy and help to improve the positioning accuracy of the airborne LiDAR remote sensing system. Through filtering and

interpolation of point clouds, three representative surface crops in the agricultural irrigation area were successfully established. Rapid detection of crop growth height could be achieved by data derived from a three-dimensional model. By extracting the characteristic line of the ecological irrigation canal, the extraction of the ecological irrigation canal is realized and the three-dimensional digital model of irrigation canal is established. The distribution of ecological irrigation canals in agricultural irrigation areas can be accurately controlled by the irrigation canal digital model. The irrigation canal size derived from the irrigation canal digital model can calculate the water transfer capacity of irrigation canals. Through the above two aspects, the supply and demand analysis and rational distribution of water resources in the whole agricultural irrigation area can be realized, which meets the needs of precision agriculture and digital agriculture. The limitation of this paper is that only the extraction experiment of the irrigation canal in a specific area is carried out. In the future, LiDAR remote sensing will be more widely used in the extraction of ecological irrigation canals and the reconstruction of crop 3D digital models. Moreover, owing to the flexibility of a multi-rotor UAV in remote sensing operations in specific areas, a multi-rotor UAV equipped with a small LiDAR or optical image remote sensing system will be more suitable for remote sensing operations in the agricultural field [54,55].

Acknowledgments

This research was supported in part by the National Key R&D Program of China (Grant Nos. 2017YFD0701003 from 2017YFD0701000, 2018YFD0700603 from 2018YFD0700600, and 2016YFD0200702 from 2016YFD0200700), by the National Natural Science Foundation of China (Grant No. 51979275), by the Jilin Province Key R&D Plan Project (Grant No. 20180201036SF), by the Open Fund of Synergistic Innovation Center of Jiangsu Modern Agricultural Equipment and Technology, Jiangsu University (Grant No. 4091600015), by the Open Research Fund of State Key Laboratory of Information Engineering in Surveying, Mapping and Remote Sensing, Wuhan University (Grant No. 19R06), by the Open Research Project of the State Key Laboratory of Industrial Control Technology, Zhejiang University (Grant No. ICT20021), and by the Chinese Universities Scientific Fund (Grant Nos. 2020TC033 and 10710301).

References

[1] J.L. Lovell, D.L.B. Jupp, D.S. Culvenor, N.C. Coops, Using airborne and ground-based ranging LiDAR to measure canopy structure in Australian forests, Can. J. Remote Sens., 29 (2003) 607–622.
[2] J.L. Lovell, D.L.B. Jupp, G.J. Newnham, D.S. Culvenor, Measuring tree stem diameters using intensity profiles from ground-based scanning LiDAR from a fixed viewpoint, ISPRS J. Photogramm. Remote Sens., 66 (2011) 46–55.
[3] A.H. Strahler, D.L.B. Jupp, C.E. Woodcock, C.B. Schaaf, T. Yao, F. Zhao, X.Y. Yang, J. Lovell, D. Culvenor, G. Newnham, W. Ni-Miester, W. Boykin-Morris, Retrieval of forest structural parameters using a ground-based LiDAR instrument (Echidna®), Can. J. Remote Sens., 34 (2008) S426–S440.
[4] B. Koetz, F. Morsdorf, G. Sun, K.J. Ranson, K. Itten, B. Allgower, Inversion of a LiDAR waveform model for forest biophysical parameter estimation, IEEE Geosci. Remote Sens. Lett., 3 (2006) 49–53.
[5] G. Zheng, L.M. Moskal, S.-H. Kim, Retrieval of effective leaf area index in heterogeneous forests with terrestrial laser scanning, IEEE Trans. Geosci. Remote Sens., 51 (2013) 777–786.
[6] C.Y. Zhang, Y.H. Zhou, F. Qiu, Individual tree segmentation from LiDAR point clouds for urban forest inventory, Remote Sens., 7 (2015) 7892–7913.
[7] L.M. Moskal, G. Zheng, Retrieving forest inventory variables with terrestrial laser scanning (TLS) in urban heterogeneous forest, Remote Sens., 4 (2012) 1–20.
[8] L.H. Jing, B.X. Hu, J.L. Li, T. Noland, Automated delineation of individual tree crowns from LiDAR data by multi-scale analysis and segmentation, Photogramm. Eng. Remote Sens., 78 (2012) 1275–1284.
[9] Z.Y. Zhang, A. Kazakova, L.M. Moskal, D.M. Styers, Object-based tree species classification in urban ecosystems using LiDAR and hyperspectral data, Forests, 7 (2016) 122.
[10] R.O. Dubayah, S.L. Sheldon, D.B. Clark, M.A. Hofton, J.B. Blair, G.C. Hurtt, R.L. Chazdon, Estimation of tropical forest height and biomass dynamics using LiDAR remote sensing at La Selva, Costa Rica, J. Geophys. Res. G: Biogeosci., 115 (2010) 272–281.
[11] M.A. Lefsky, W.B. Cohen, T.A. Spies, An evaluation of alternate remote sensing products for forest inventory, monitoring, and mapping of Douglas-fir forests in western Oregon, Can. J. For. Res., 31 (2001) 78–87.
[12] Z.S. Wang, C.B. Schaaf, P. Lewis, Y. Knyazikhin, M.A. Schull, A.H. Strahler, R.B. Myneni, M.J. Chopping, B.J. Blair, Retrieval of canopy height using moderate-resolution imaging spectroradiometer (MODIS) data, Remote Sens. Environ., 115 (2011) 1595–1601.
[13] C. Alexander, A.H. Korstjens, R.A. Hill, Influence of micro-topography and crown characteristics on tree height estimations in tropical forests based on LiDAR canopy height models, Int. J. Appl. Earth Obs. Geoinf., 65 (2018) 105–113.
[14] M.W. He, H.J. Zhao, F. Davoine, J.S. Cui, H.B. Zha, Pairwise LiDAR Calibration Using Multi-Type 3D Geometric Features in Natural Scene, IEEE/RSJ International Conference on Intelligent Robots and Systems, Tokyo, Japan, 3–7 November 2013.
[15] J.-H. Song, S.-H. Han, K. Yu, Y.-I. Kim, Assessing the possibility of land-cover classification using LiDAR intensity data, Int. Soc. Photogramm. Remote Sens., 34 (2012) 9–13.
[16] C.X. Cao, M. Xu, Y.F. Bao, H. Zhang, Synchronous Retrieval of Forest Canopy Cover by Airborn LiDAR and Optical Remote Sensing, IEEE International Geoscience and Remote Sensing Symposium, Honolulu, HI, USA, 25–30 July 2010.
[17] I. Fayad, N. Baghdadi, J.S. Bailly, N. Barbier, V. Gond, B. Hérault, M. El Hajj, J. Lochard, J. Perrin, Regional Scale Rain-Forest Height Mapping Using Regression-Kriging of Spaceborne and Airborne LiDAR Data: Application on French Guiana, IEEE International Geoscience and Remote Sensing Symposium (IGARSS), Milan, Italy, 26-31 July 2015.
[18] X.Y. Wang, D.H. Xie, G.J. Yan, W.M. Zhang, Y. Wang, Y.M. Chen, 3D Reconstruction of a Single Tree From Terrestrial LiDAR Data, IEEE Geoscience and Remote Sensing Symposium, Quebec City, QC, Canada, 13–18 July 2014, pp. 796–799.
[19] H.B. Xiang, C.X. Cao, H.C. Jia, M. Xu, R.B. Myneni, The Analysis on the Accuracy of DEM Retrieval by the Ground LiDAR Point Cloud Data Extraction Methods in Mountain Forest Areas, IEEE International Geoscience and Remote Sensing Symposium, Munich, Germany, 22–27 July 2012, pp. 6067–6070.
[20] C. Paris, L. Bruzzone, A growth-model-driven technique for tree stem diameter estimation by using airborne LiDAR data, IEEE Trans. Geosci. Remote Sens., 57 (2019) 76–92.
[21] J.F. Wu, H.L. Wang, N. Li, P. Yao, Y. Huang, Z.K. Su, Y. Yu, Distributed trajectory optimization for multiple solar-powered UAVs target tracking in urban environment by Adaptive Grasshopper Optimization Algorithm, Aerosp. Sci. Technol., 70 (2017) 497–510.
[22] Y. Yu, H.L. Wang, X.L. Shao, Y. Huang, The Attitude Control of UAV in Carrier Landing Based on ADRC, IEEE Chinese Guidance, Navigation and Control Conference, Nanjing, China, 12–14 Aug 2016, pp. 832–837.

[23] Z.B. Zhou, L. Yang, Y. Li, An Adaptive Dual Kalman Filtering Algorithm for Locata/GPS/INS Integrated Navigation, 4th China Satellite Navigation Conference (CSNC) 2013 Proceedings, Wuhan, China, 13–17 May 2013, pp. 527–541.
[24] M.-J. Yu, INS/GPS integration system using adaptive filter for estimating measurement noise variance, IEEE Trans. Aerosp. Electron. Syst., 48 (2012) 1786–1792.
[25] J.B. Wu, An Innovative Neural-Fuzzy Adaptive Kalman Filter for Ultra-Tightly Coupled GPS/INS Integrated System, Beijing Institute of Remote Sensing Equipment, Beijing, China, 2017.
[26] R. Babu, J.L. Wang, Ultra-tight GPS/INS/PL integration: a system concept and performance analysis, GPS Solutions, 13 (2009) 75–82.
[27] L. Zhao, H.Y. Qiu, Y.M. Feng, Analysis of a robust Kalman filter in loosely coupled GPS/INS navigation system, Measurement, 80 (2016) 138–147.
[28] G.Q. Wang, Y. Han, J. Chen, S.B. Wang, Z.C. Zhang, N. Du, Y.J. Zheng, A GNSS/INS integrated navigation algorithm based on Kalman filter, IFAC-PapersOnLine, 51 (2018) 232–237.
[29] N.C. Yadav, A. Shanmukha, B.M. Amruth, Basavaraj, Development of GPS/INS Integration Module Using Kalman Filter, International Conference on Algorithms, Methodology, Models and Applications in Emerging Technologies, Chennai, India, 16–18 February 2017.
[30] Y. Zhou, C. Zhang, Y.F. Zhang, J.Z. Zhang, A new adaptive square-root unscented Kalman filter for nonlinear systems with additive noise, Int. J. Aerosp. Eng., 2015 (2015), https://doi.org/10.1155/2015/381478.
[31] O. Derbel, M.L. Cherif, R. Landry Jr., Driver Behavior Assessment Based on Loosely Coupled GPS/INS Integration in Harsh Environment, IEEE/ION Position, Location and Navigation Symposium, Monterey, CA, USA, 23–26 April. 2018, pp. 1362–1367.
[32] S.H. Oh, D.-H. Hwang, Low-cost and high performance ultra-tightly coupled GPS/INS integrated navigation method, Adv. Space Res., 60 (2017) 2691–2706.
[33] R. Chen, K-Means Aided Kalman Filter Noise Estimation Calibration for Integrated GPS/INS Navigation, IEEE International Conference on Intelligent Transportation Engineering, Singapore, 20–22 August 2016, pp. 156–161.
[34] I.-U. Lee, H. Li, N.-M. Hoang, J.-M. Lee, Navigation System Development of the Underwater Vehicles Using the GPS/INS Sensor Fusion, 14th International Conference on Control, Automation and Systems, Seoul, South Korea, 22–25 October 2014, pp. 610–612.
[35] C. Liu, H.L. Wang, N. Li, Y. Yu, Sensor Fault Diagnosis of GPS/INS Tightly Coupled Navigation System Based on State Chi-square Test and Improved Simplified Fuzzy ARTMAP Neural Network, IEEE International Conference on Robotics and Biomimetics (ROBIO), Macau, China, 5–8 December 2017, pp. 2527–2532.
[36] R. Eberhart, J. Kennedy, A New Optimizer Using Particle Swarm Theory, Proceedings of the Sixth International Symposium on Micro Machine and Human Science, Nagoya, Japan, Japan, 4–6 October 1995, pp. 39–43.
[37] O.P. Rahi, A.K. Chandel, M.G. Sharma, Optimization of Hydro Power Plant Design by Particle Swarm Optimization (PSO), Procedia Eng., 30 (2012) 418–425.
[38] A. Jaini, I. Musirin, N. Aminudin, M.M. Othman, T.K.A. Rahman, Particle Swarm Optimization (PSO) Technique in Economic Power Dispatch Problems, 4th International Power Engineering and Optimization Conference, Shah Alam, Malaysia, 23–24 June 2010, pp. 308–312.
[39] K.M. Gharaibeh, A. Yaqot, Target Classification in Wireless Sensor Network Using Particle Swarm Optimization (PSO), 2012 IEEE Sensors Applications Symposium Proceedings, Brescia, Italy, 7–9 February 2012.
[40] Y. Marinakis, M. Marinaki, G. Dounias, A hybrid particle swarm optimization algorithm for the vehicle routing problem, Eng. Appl. Artif. Intell., 23 (2010) 463–472.
[41] S.H. Cai, M.L. Li, Cost optimization problem of hybrid flow-shop based on PSO algorithm, Adv. Mater. Res., 532 (2012) 1616–1620.
[42] L.D. Li, X.H. Yu, X.D. Li, W. Guo, A Modified PSO Algorithm for Constrained Multi-objective Optimization, 2009 Third International Conference on Network and System Security, Gold Coast, QLD, Australia, 19–21 October 2009, pp. 462–467.
[43] C.-A. Liu, "New Dynamic Constrained Optimization PSO Algorithm, 2008 Fourth International Conference on Natural Computation, Jinan, China, 18–20 October 2008, pp. 650–653.
[44] J.H. Qu, Z.Z. Shao, X.Y. Liu, PSO clustering algorithm based on cooperative evolution, J. Donghua Univ. (English Edition), 27 (2010) 285–288.
[45] C.M. Gu, Y. Liu, D.B. Liu, Z.G. Li, I. Mohamed, R.H. Zhang, M. Brooks, F. Chen, Distribution and ecological assessment of heavy metals in irrigation channel sediments in a typical rural area of south China, Ecol. Eng., 90 (2016) 466–472.
[46] M.B. Huang, T.H. Dang, J. Gallichand, M. Goulet, Effect of increased fertilizer applications to wheat crop on soil-water depletion in the loess plateau, china, Agric. Water Manage., 58 (2003) 267–278.
[47] F.-M. Li, P. Wang, J. Wang, J.-Z. Xu, Effects of irrigation before sowing and plastic film mulching on yield and water uptake of spring wheat in semiarid Loess Plateau of China, Agric. Water Manage., 67 (2004) 77–88.
[48] S. Kaneko, K. Tanaka, T. Toyota, S. Managi, Water efficiency of agricultural production in china: regional comparison from 1999 to 2002, Int. J. Agric. Resour. Governance Ecol., 3 (2004) 231–251.
[49] P.C. Phondani, A. Bhatt, E. Elsarrag, Y.M. Alhorr, A. El-Keblawy, Criteria and indicator approach of global sustainability assessment system for sustainable landscaping using native plants in Qatar, Ecol. Indic., 69 (2016) 381–389.
[50] B. Das, A. Singh, S.N. Panda, H. Yasuda, Optimal land and water resources allocation policies for sustainable irrigated agriculture, Land Use Policy, 42 (2015) 527–537.
[51] Z. Wang, D. Zerihun, J. Feyen, General irrigation efficiency for field water management, Agric. Water Manage., 30 (1996) 123–132.
[52] H. Ali, L.T. Shui, K.C. Yan, A.F. Eloubaidy, K.C. Foong, Modeling water balance components and irrigation efficiencies in relation to water requirements for double-cropping systems, Agric. Water Manage., 46 (2000) 167–182.
[53] C. Qian, W.Y. Lin, J.H. Chen, Z. Li, H.J. Gao, Point Cloud Trajectory Planning Based on Octree and K-dimensional Tree Algorithm, 31st Youth Academic Annual Conference of Chinese Association of Automation (YAC), Wuhan, China, 11–13 November 2016, pp. 213–218.
[54] Z.C. Zhang, Y. Han, J. Chen, S.B. Wang, G.Q. Wang, N.N. Du, Information extraction of ecological canal system based on remote sensing data of unmanned aerial vehicle, J. Drain. Irrig. Mach. Eng., 36 (2018) 1006–1011.
[55] S.B. Wang, Y. Han, J. Chen, Y. Pan, Y. Cao, H. Meng, Weed classification of remote sensing ecological irrigation area by UAV based on deep learning, J. Drain. Irrig. Mach. Eng., 11 (2018) 1137–1141.